



**HAL**  
open science

## **Altiratinib blocks *Toxoplasma gondii* and *Plasmodium falciparum* development by selectively targeting a spliceosome kinase**

Christopher Swale, Valeria Bellini, Matthew Bowler, Nardella Flore, Marie-Pierre Brenier-Pinchart, Dominique Cannella, Lucid Belmudes, Caroline Mas, Yohann Couté, Fabrice Laurent, et al.

### ► To cite this version:

Christopher Swale, Valeria Bellini, Matthew Bowler, Nardella Flore, Marie-Pierre Brenier-Pinchart, et al.. Altiratinib blocks *Toxoplasma gondii* and *Plasmodium falciparum* development by selectively targeting a spliceosome kinase. *Science Translational Medicine*, 2022, 14 (656), 17 p. 10.1126/scitranslmed.abn3231 . hal-03752215

**HAL Id: hal-03752215**

**<https://hal.inrae.fr/hal-03752215>**

Submitted on 5 Sep 2022

**HAL** is a multi-disciplinary open access archive for the deposit and dissemination of scientific research documents, whether they are published or not. The documents may come from teaching and research institutions in France or abroad, or from public or private research centers.

L'archive ouverte pluridisciplinaire **HAL**, est destinée au dépôt et à la diffusion de documents scientifiques de niveau recherche, publiés ou non, émanant des établissements d'enseignement et de recherche français ou étrangers, des laboratoires publics ou privés.



Distributed under a Creative Commons Attribution - NonCommercial - NoDerivatives 4.0 International License

1  
2           Altiratinib blocks *Toxoplasma gondii* and *Plasmodium*  
3           *falciparum* development by selectively targeting  
4           a spliceosome kinase

5  
6 Christopher Swale<sup>1†\*</sup>, Valeria Bellini<sup>1†</sup>, Matthew W. Bowler<sup>2</sup>, Nardella Flore<sup>3</sup>, Marie-Pierre  
7 Brenier-Pinchart<sup>1</sup>, Dominique Cannella<sup>1</sup>, Lucid Belmudes<sup>4</sup>, Caroline Mas<sup>5</sup>, Yohann Couté<sup>4</sup>,  
8 Fabrice Laurent<sup>6</sup>, Artur Scherf<sup>3</sup>, Alexandre Bougdour<sup>1\*</sup> and Mohamed-Ali Hakimi<sup>1\*</sup>  
9

10 <sup>1</sup> Institute for Advanced Biosciences (IAB), Team Host-pathogen interactions and immunity to  
11 infection, INSERM U1209, CNRS UMR5309, University Grenoble Alpes, Grenoble, France

12 <sup>2</sup> European Molecular Biology Laboratory, Grenoble, 71 Avenue des Martyrs, CS 90181,  
13 38042 Grenoble, France.

14 <sup>3</sup> Institut Pasteur, Université de Paris, Unité de Biologie des Interactions Hôte-Parasite, CNRS  
15 ERL 9195, INSERM U1201, F-75015 Paris, France.

16 <sup>4</sup> Univ. Grenoble Alpes, INSERM, CEA, UMR BioSanté U1292, CNRS, CEA, FR2048  
17 38000, Grenoble, France.

18 <sup>5</sup> Integrated Structural Biology Grenoble (ISBG) CNRS, CEA, Université Grenoble Alpes,  
19 EMBL, 71 avenue des Martyrs, F-38042, Grenoble, France.

20 <sup>6</sup> INRAE, Université François Rabelais de Tours, Centre Val de Loire, UMR1282 ISP,  
21 Laboratoire Apicomplexes et Immunité Mucosale, 37380 Nouzilly, France.

22  
23 †These authors contributed equally to this work.

24  
25 \* Correspondence to:

26 [mohamed-ali.hakimi@univ-grenoble-alpes.fr](mailto:mohamed-ali.hakimi@univ-grenoble-alpes.fr) - ORCID: 0000-0002-2547-8233

27 [alexandre.bougdour@univ-grenoble-alpes.fr](mailto:alexandre.bougdour@univ-grenoble-alpes.fr) - ORCID: 0000-0002-5895-0020

28 [christopher.swale@univ-grenoble-alpes.fr](mailto:christopher.swale@univ-grenoble-alpes.fr) - ORCID: 0000-0002-9739-7774  
29

30 **Spliceosome targeting by altiratinib leads to *Toxoplasma* and *Plasmodium* inhibition.**  
31

32 **Key words:** *Toxoplasma gondii*, *Plasmodium falciparum*, drug repurposing, kinase, splicing

33

## 34 **Abstract**

35 The apicomplexa comprise a large phylum of single-celled, obligate intracellular protozoa that  
36 include *Toxoplasma gondii*, *Plasmodium* and *Cryptosporidium spp* which infect humans and  
37 animals and cause severe parasitic diseases. Available therapeutics against these diseases are  
38 limited by suboptimal efficacy and frequent side effects, as well as the emergence and spread  
39 of resistance. We use a drug repurposing strategy and identified altiratinib, a compound  
40 originally developed to treat glioblastoma, as a promising drug candidate with broad spectrum  
41 activity against apicomplexans. Altiratinib is parasiticidal and blocks the development of  
42 intracellular zoites in the nanomolar range and with a high selectivity index when used against  
43 *T. gondii*. We have identified *TgPRP4K* of *T. gondii* as the primary target of altiratinib using  
44 genetic target deconvolution, which highlighted key residues within the kinase catalytic site  
45 that conferred drug resistance when mutated. We have further elucidated the molecular basis of  
46 the inhibitory mechanism and species selectivity of altiratinib for *TgPRP4K* as well as for its  
47 *P. falciparum* counterpart, *PfCLK3*. Our data identified structural features critical for binding  
48 of the other *PfCLK3* inhibitor, TCMDC-135051. Consistent with the splicing control activity  
49 of this kinase family, we have shown that altiratinib can causes global disruption of splicing,  
50 primarily through intron retention in both *T. gondii* and *P. falciparum*. Thus, our data establish  
51 parasitic PRP4K/CLK3 as a potential pan-apicomplexan target whose repertoire of inhibitors  
52 can be expanded by the addition of altiratinib.

53

## 54 **Introduction**

55 Infectious diseases caused by apicomplexan parasites remain one of the leading causes of  
56 morbidity and mortality around the world, with even more devastating consequences in low-  
57 income countries, underscoring the need for effective medicines. *Plasmodium falciparum*  
58 causes malaria in over 240 million people worldwide and is responsible for more than 627 000  
59 deaths in 2020 (1). Similarly, *Toxoplasma gondii*, the causative agent of toxoplasmosis, causes  
60 widespread zoonotic infection, with nearly one-third of the world's population being  
61 seropositive for this parasite. In healthy adults, the acute infection resolves rapidly, leaving a  
62 chronic, subclinical infection in some individuals. In the absence of sustained immunity,  
63 reactivation of latent forms of *T. gondii* leads to severe, life-threatening disease, as has been  
64 observed in AIDS, organ transplant and chemotherapy patients, with a high mortality rate in

65 the absence of treatment (2). More severe cases may also occur following congenital  
66 transmission of the parasite to an unborn child. In addition, *Toxoplasma gondii*, together with  
67 other coccidian parasites, e.g. *Eimeria* spp. And *Neospora caninum*, are of veterinary  
68 importance as they cause significant economic losses in livestock populations.

69  
70 For many of these apicomplexa-mediated diseases, current treatments are suboptimal, and for  
71 some there are few, if any, alternatives. The current standard treatment of toxoplasmosis is  
72 based on a pyrimethamine-sulfadiazine combination but is hampered by severe side effects,  
73 especially in immunocompromised individuals (3). For malaria, artemisinin-based combination  
74 therapies (ACT) are currently used as first-line treatments in endemic countries worldwide, but  
75 the emergence and spread of resistance not only to artemisinin but also to other drug  
76 combinations is a growing threat (1). The ever-present threats of drug resistance have led to the  
77 search for other therapeutic alternatives. Older drugs have recently made a comeback by being  
78 repurposed for new diseases to accelerate drug development (4, 5). After phenotypic screening  
79 for drug repurposing, new indications for existing drugs can be quickly identified and clinical  
80 trials can be rapidly conducted. Identifying the target and understanding the mechanism of  
81 action are critical bottlenecks in drug development, as these two phases provide the essential  
82 chemical basis for targeted inhibition and pave the way for chemical derivatization of the  
83 original drug candidate. Recent advances in genomics and target deconvolution strategies have  
84 addressed these problems and have ushered in a plethora of putative targets awaiting  
85 clarification.

86  
87 Here, we report the identification of altiratinib from a chemical library that includes FDA-  
88 approved or phase I/ II clinical trial candidate drugs. Altiratinib exhibited potent, nanomolar,  
89 broad-spectrum anti-apicomplexan activity with a high selectivity index and had previously  
90 been in phase 1 clinical development for the treatment of invasive solid tumors, including  
91 glioblastoma (6, 7). Using a genetic target deconvolution strategy, we identified *T. gondii*  
92 *TgPRP4K*, the closest relative of the human splicing factor kinase PRP4 kinase  
93 (PRP4K/PRPF4B) and *Plasmodium falciparum* *PfCLK3* (8, 9), as the primary target of  
94 altiratinib. In addition, we used an integrated structural biology approach to further elucidate  
95 the molecular basis of the mechanism of inhibition of altiratinib and characterized the  
96 remarkable selectivity of this drug for parasitic PRP4K/CLK3 enzymes. This kinase family  
97 plays a critical role in cell cycle progression by regulating pre-mRNA splicing in all eukaryotic  
98 lineages (10-13). Accordingly, altiratinib caused global disruption of splicing with exon

99 skipping, intron retention, and premature transcription termination in both *T. gondii* and *P.*  
100 *falciparum*, but not in *Cryptosporidium parvum*, in which the kinase has significantly divergent  
101 variations that may result in resistance to altiratinib. Our findings support this family of parasitic  
102 kinases as a promising apicomplexan target and highlight the structural determinants that  
103 explain the remarkable selectivity of altiratinib.

104

## 105 **Results**

### 106 **A drug repurposing screen identifies altiratinib as a potent and selective apicomplexan** 107 **inhibitor of parasite growth**

108 To identify new drug candidates against toxoplasmosis and potential targets, we screened a  
109 small library of 514 approved drugs or drugs undergoing clinical trials for their ability to inhibit  
110 *T. gondii* tachyzoite growth. All compounds are structurally diverse, cell permeable, medically  
111 active, and commercially available (Table S1). Screening was performed in duplicate at 5  $\mu$ M  
112 while pyrimethamine was used as a reference drug and blocked the growth of type I (RH)  
113 parasites as expected. The compounds that showed reproducible inhibition of parasite growth  
114 of >70% were selected for further testing (Fig. S1A; Table S1). Of the 514 compounds in the  
115 collection, 75 primary hits were found to inhibit parasite growth without detectable cytotoxicity  
116 to the host cell (Fig. 1A), preferentially targeting the cell cycle and tyrosine kinase/adaptor  
117 signaling pathways (Fig. S1B; Table S1). A second screen at 1  $\mu$ M of the 84 compounds  
118 identified 14 molecules with EC<sub>50</sub> in the nM range (Fig. 1B; Fig. S2). The most potent growth  
119 inhibitor we identified was altiratinib (DCC-2701, DP-5164, Fig. 1C) with an EC<sub>50</sub> of 28 nM  
120 against tachyzoites, which is 11-fold lower than pyrimethamine (300 nM), the standard  
121 treatment for toxoplasmosis (Fig. 1D). Altiratinib-treated parasites were smaller than the  
122 control group and no longer divided, as no daughter cells were detectable (Fig. 1E). Plaque  
123 assays showed sustained inhibition of parasite growth, as plaques could no longer be detected  
124 in the presence of altiratinib, suggesting a defect in one or more steps of the lytic cycle (Fig.  
125 S3). Interestingly, we did not observe regrowth within 6 to 10 days after discontinuation of  
126 altiratinib, suggesting that the drug has a cidal effect in contrast to pyrimethamine (Fig. S3).  
127 Altiratinib also showed low host cytotoxicity compared with THZ1 used as a cytotoxic control  
128 (Fig. S1D), resulting in a high selectivity index (SI) with a value of 400 for human primary  
129 fibroblasts (Fig. 1F). Altiratinib was also effective in inhibiting the growth of coccidial parasites  
130 of veterinary importance such as *Eimeria tenella* (Fig. 1G) and *Neospora caninum* (Fig. 1H),

131 as well as *P. falciparum*, although its efficacy is lower compared with the antimalarial drug  
132 dihydroartemisinin (DHA) (Fig. 1i).

133

### 134 **Altiratinib target deconvolution by EMS-based forward genetic screen identifies** 135 ***TgPRP4K* as a resistance gene**

136 Altiratinib was originally identified to inhibit tumor growth and invasion in a bevacizumab-  
137 resistant glioblastoma mouse model and was in phase 1 clinical development for the treatment  
138 of invasive solid tumors. The drug was predicted to be a pan-tyrosine kinase inhibitor of MET,  
139 TIE2, VEGFR2, and TRK (6, 7), but none of these kinases are conserved in apicomplexa.  
140 Therefore, to explore the mechanism of action of altiratinib in *T. gondii*, we performed a  
141 forward genetic screen combining chemical mutagenesis and RNA sequencing, as previously  
142 described (14) (Fig. S1E). Altiratinib-resistant parasites were generated in 6 independent  
143 chemical mutagenesis experiments using 2.5 mM ethyl methanesulfonate (EMS) followed by  
144 selection in the presence of 300 nM altiratinib, i.e. 10-fold the EC<sub>50</sub> value, for approximately 4  
145 weeks. The resistant parasite lines were then cloned by limited dilution, and a single clone from  
146 each mutagenesis experiment (designated A to F) was analyzed by whole-genome RNA  
147 sequencing (RNA-Seq). To map the EMS-induced mutations conferring resistance to  
148 altiratinib, Illumina sequencing reads were aligned to the *T. gondii* *GT1* reference genome.  
149 Using the parental strain as a reference, single nucleotide variants (SNVs) were identified in  
150 the assembled sequences of the resistant mutants (see *Materials and Methods*). By focusing on  
151 mutations in coding sequences, a single gene, *TGGT1\_313180*, contained SNVs that resulted  
152 in amino acid changes (F647S, L686F, L715F) not present in the parental strain in five of the  
153 six drug-resistant lines (Fig. 2, A and B; Table S2).

154

155 *TGGT1\_313180* encodes a 928 amino acid (aa) protein that has a predicted kinase domain in  
156 its C-terminus, hereafter referred to as *TgPRP4K* (Fig. 2B). *TgPRP4K* is phylogenetically  
157 related to the cyclin-dependent-like kinase family (CLK) (15, 16) and its closest homolog in  
158 humans is the splicing factor kinase PRP4 kinase (PRP4K or PRPF4B) and in *P. falciparum* is  
159 *PfCLK3* (*PF3D7\_1114700*), a kinase that has been identified as a multistage cross-species  
160 antimalarial drug target (Fig. S4A) (8, 9, 17). Immunofluorescence analysis of intracellular  
161 parasites showed that *TgPRP4K* is localized to nuclear speckle-like structures (Fig. 2C).  
162 *TgPRP4K* is essential for the lytic cycle of tachyzoites, as its genetic disruption results in a  
163 fitness score of -4.69 (18), and conditional knockdown of the kinase using the auxin-inducible

164 degon system (AID) dramatically impaired parasite growth (Fig. 2D) in agreement with a  
165 recent study (19).

166

167 Surprisingly, the altiratinib-resistant parasite line from mutagenesis F has a wild-type (WT)  
168 allele of *TgPRP4K* and a mutation E1325K in *TgPRP8*, a protein located in the catalytic core  
169 of the spliceosome that has been shown to interact with PRP4K in *Schizosaccharomyces pombe*  
170 to facilitate spliceosome activation (20, 21). This reinforces the possibility that the PRP4K-  
171 PRP8 complex is at the basis for the anti-*Toxoplasma* activity of altiratinib. The specific  
172 association between *TgPRP4K* and *TgPRP8* was then confirmed by FLAG affinity  
173 immunoprecipitation and mass spectrometry (MS)-based proteomic analyzes using knock-in  
174 parasite lines expressing a tagged version of each protein (Table S3; Fig. S4, B and C). Other  
175 partners have been identified as pre-mRNA splicing proteins constitutive of the core  
176 spliceosome, such as U2 snRNP proteins and U5 snRNP proteins, including the RNA helicase  
177 Brr2 and Snu114, which forms a pocket enclosing the catalytic RNA network of activated  
178 spliceosomes (Fig. S5) (21, 22). Known pre-mRNA splicing factors were also purified along  
179 with PRP4K and PRP8 (Table S3; Fig. S4, B and C; Fig. S5). *TgPRP4K* was found in a high  
180 molecular-weight complex (~500 kDa; fractions 24–26) that withstood stringent salt conditions  
181 and partially co-eluted with the *TgPRP8*-containing spliceosome, which migrates by size  
182 exclusion chromatography with an apparent molecular weight of ~900 kDa (fractions 18-20)  
183 (Fig. S4, B and C).

184

### 185 **Single mutations within *TgPRP4K* confer resistance to altiratinib**

186 To confirm that the mutations found in *TgPRP4K* and *TgPRP8* were sufficient to confer  
187 resistance to altiratinib, we used the CRISPR/Cas9 system in conjunction with homology-  
188 directed repair, to reconstruct each of the etiological mutations into the susceptible parental *T.*  
189 *gondii* strain (14). Parasites were cotransfected with a vector expressing the Cas9 endonuclease  
190 and a synthetic guide RNA (sgRNA) targeting either *TgPRP4K* or *TgPRP8*, and the  
191 corresponding homologous single-stranded donor oligonucleotides (ssODN) as repair  
192 templates (Fig. S6A). After altiratinib selection, the resistant parasites were cloned, and DNA  
193 sequencing confirmed that the mutations were properly introduced at the *TgPRP4K* locus (Fig.  
194 S6B). Note that despite numerous attempts, allelic substitution for *TgPRP8* could not be  
195 achieved, suggesting that the *TgPRP8* (E1325K) mutation alone does not confer resistance to  
196 altiratinib and was not investigated further. Compared with WT parasites, mutant strains edited

197 for *TgPRP4K* (mutations F647S, L686F, and L715F) significantly decreased sensitivity to  
198 altiratinib by 50- to 180-fold (Fig. 2, E to G; Fig. S6C), suggesting that resistance to altiratinib  
199 correlates with *TgPRP4K* activity. In addition, the CRISPR/Cas9-edited lines had altiratinib  
200 resistance levels at least as high as the EMS-mutagenized clones (Fig. S7; Table S2). This  
201 suggests that the reconstructed *TgPRP4K* mutations fully recapitulate the resistance phenotype  
202 originally observed in the mutagenized lines, and that it is unlikely that other secondary  
203 mutations are involved in the resistance mechanism. It is worth noting that the CRISPR/Cas9-  
204 edited parasite with the F647S mutation exhibited a higher level of resistance to altiratinib than  
205 its mutant counterpart, most likely due to overall growth failure of the latter (Fig. S7).

206

### 207 **Structural studies uncover the mechanism of action of altiratinib on *TgPRP4K***

208 To unravel the molecular mechanism of action of altiratinib inhibition, we expressed the  
209 predicted kinase domain of *TgPRP4K* in the WT and L715F variant versions by removing the  
210 intrinsically disordered region at the N-terminus (Fig. S8A). Both recombinant proteins were  
211 produced in satisfactory yields, with the notable difference being a higher size homogeneity of  
212 the L715F mutant (Fig. S8B) when analyzed by size exclusion chromatography coupled to laser  
213 light scattering (SEC-MALLS). The same sample did not display a double band that can be  
214 seen in the WT (Fig. S8C) and was also observed in Flag-purified human WT PRPF4B as a  
215 result of posttranslational modifications (23). The L715F mutation is peculiar because it  
216 centered on the DFG (Asp-Phe-Gly) motif, which is a DLG (Asp-Leu-Gly) in apicomplexan  
217 parasites. DFG (or DLG in a subset of kinases, such as RIPK1) is a highly conserved peptidic  
218 motif found in most human kinases and is critical for allosteric placement of the activation loop.  
219 Using a thermal stability assay and a thermophoresis titration assay, we could show a direct  
220 stabilizing effect ( $\Delta T_m$  of 11 °C) and binding (apparent  $K_d$  of 64 nM) of altiratinib with the  
221 WT *TgPRP4K* kinase domain (Fig. 3, A and B). Counterintuitively though, the L715F mutation  
222 does not decrease altiratinib binding, but instead increases binding affinity (Fig. 3, A and B).  
223 This not only increases the apparent  $K_d$  value (26 nM), but also increases the stabilizing effect  
224 of the compound *in vitro* compared to WT (with a  $\Delta T_m$  of 15 °C). This surprising observation  
225 highlights an unusual resistance mechanism that should somehow compensate for the inhibitory  
226 mechanism, regardless of the binding affinity of the compound. Using this point mutant, we  
227 successfully co-crystallized *TgPRP4K* in complex with altiratinib and obtained high-resolution  
228 diffraction to 2.3 Å (pdb id: 7Q4A, Table S4). A molecular replacement solution was found with  
229 the human homolog of PRPF4B kinase domain (pdb id: 6CNH), which shares 47% sequence



230 identity with *TgPRP4K*. The structure solution showed *TgPRP4K* crystallizing as a dimer with  
231 the catalysis cavities facing each other (Fig. S9A). The monomer B exhibited more complete  
232 density within the flexible regions, so all further structural representations are based on this  
233 monomer. The activation loop was fully assembled in our model and occupies a DFG “out”  
234 conformation while the tyrosine 729 is phosphorylated in this structure (Fig. 3C, Fig. S9B and  
235 C). Interestingly, this phospho-tyrosine is central to the ability of *TgPRP4K* to crystallize under  
236 these conditions, as it forms numerous crystal contacts with other symmetry-related molecules  
237 (Fig. S9B).

238  
239 The activation loop displays an alpha helix (Ile 726 to Tyr 735) that appears to be unique to *T.*  
240 *gondii* PRP4K when compared to the human ortholog, which was only ever crystallized in DFG  
241 “in” conformations and is largely a random coil in this state (Fig. 3C, Fig. S9C). Compared to  
242 the human ortholog in its global structure, *TgPRP4K* is structurally conserved, with minor  
243 structural differences in the C-terminal portion (aa 840 to 854) of the kinase domain (Fig. S9C).  
244 The structure also reveals a C-terminal antiparallel short beta strand that, to our knowledge, is  
245 unique to the PRP4K kinase lineage (Fig. 3C) and is also structurally conserved in the human  
246 ortholog (Fig. S9C), although sequence conservation for this region is very low.

247  
248 Electron density for altiratinib was clearly visible in our crystal structure and interacts in the  
249 ATP-binding pocket located at the interface between the N- and C-lobes (Fig. 3C), with the  
250 DFG motif and the G-rich loop closing off this cavity. It is noteworthy that both monomers  
251 display strong electron density for altiratinib, allowing us to confidently assign the entire  
252 molecule (Fig. S10A). More detailed analysis revealed that the interaction of the compound  
253 within the cavity relies on numerous hydrophobic interactions (Fig. 3D; Fig. S10, B and C),  
254 which can be divided into three distinct zones. The first zone, consisting of a cyclopropane-  
255 carbonylamino group connecting a pyridine ring, interacts mainly with side chains W649, L650,  
256 W651, L702 and A595 (Fig. 3D, Fig. S10C). Hydrogen bonds also form with the carbonyl and  
257 amide groups of the leucine 650, and most of these residues form the ATP-binding hinge region,  
258 leading to the deeper allosteric pocket. The second zone of altiratinib is central and consists  
259 mainly of a difluorophenyl ring stacked between the two phenylalanines 647 and 715 (the DFG  
260 central residue, which is a leucine in wild type *TgPRP4K*) (Fig. 3D), with one of the fluorine  
261 groups interacting with the sulfur group of C713 (Fig. S10C). These interactions ensure that the  
262 activation loop remains in this « out » position. Finally, the last part of altiratinib which

263 encompasses a cyclopropane-1,1-dicarboxamide leading to a fluorophenyl ring, is buried deep  
264 in the allosteric cavity and interacts with multiple residues within the C-lobe, notably the  
265 glutamic acid 612 and leucine 616 and 619, which line up on the C-alpha-helix (Fig. 3D, Fig.  
266 S10C). Other interactions are mediated by I630 and L686, as well as the H693, which belongs  
267 to the canonical HxD triad that is a H/A/D in PRP4K proteins. Only one residue within the N-  
268 lobe, the catalytic lysine K597, forms a hydrogen bond with the central carboxy group. Using  
269 this structure, we can now rationalize the consequences of the resistance mutations triggered by  
270 our EMS screen. All of the point mutations we obtained involve residues that interact directly  
271 with altiratinib, whereas the direct mechanisms of resistance are likely quite different (Fig. 3E).  
272 The L686F mutation logically introduces a steric hindrance for the fluorophenyl ring by  
273 significantly increasing the size of the side-chain. The other two resistance-conferring  
274 mutations, F647S and L715F, involve residues in direct interaction and at opposite sides of the  
275 central difluorophenyl ring. F647S probably strongly decreases hydrophobic stacking, while  
276 we have evidence that the mutation L715F does not cause steric hindrance but, on the contrary,  
277 probably increases hydrophobic stacking of the difluorophenyl ring. As such, most of the  
278 mutated residues are highly conserved elements found in both *HsPRPF4B* and *TgPRP4K* (the  
279 L715F is a significant divergence but does not negatively affect compound binding) and are  
280 unlikely to be involved in interspecies binding selectivity. Altiratinib is not recognized as an  
281 inhibitor of PRPF4B in human cells, as it was originally designed to inhibit the kinases MET,  
282 TIE2 (TEK), and VEGFR2 (KDR) (6, 7). Of the residues involved in binding to altiratinib,  
283 most are strictly conserved among PRPF4B orthologs (Fig. 3E), but the hinge region has  
284 residues (W649 and W651) that diverge considerably from the human ortholog, being replaced  
285 by a proline and serine, respectively.

286

### 287 **Hinge region residue 649 controls species specificity of altiratinib towards *TgPRP4K***

288 The superposition of the human and *T. gondii* PRPF4B/PRP4K structures makes it clear that  
289 the hinge region has a consistent backbone structure despite significant differences in side chain  
290 composition (Fig. 4A). More importantly, this overlay shows that the change from W649 to  
291 P769 would affect the main hydrophobic component that stacks the cyclopropane-  
292 carbonylamino and pyridin groups of altiratinib. A similar, albeit lesser, role can also be  
293 attributed to W651, whose equivalent residue in humans is S771 and likely reduces the  
294 hydrophobic caging potential toward altiratinib. To test the significance of residue W649, we  
295 used the same CRISPR-Cas9 complementation approach for SNV validation to generate a  
296 “humanized” mutant W649/P that requires a codon change from TGG to CCG (Fig. 4B). The

297 probability of such a change occurring in EMS mutagenesis is low because it requires a  
298 simultaneous alteration of two nucleotides. This substitution is not prevalent in EMS  
299 mutagenesis, which preferentially alkylates G residues (24). Interestingly, this artificial  
300 humanization produced parasites that were resistant to altiratinib (Fig. 4, C to E) and had an  
301 EC50 of 3.5  $\mu$ M, which is comparable to the mutations using the EMS approach. Using  
302 *TgPRP4K* WT, L715F and W649P expressed in insect cells, we were able to probe the *in vitro*  
303 consequences of these two different mutations on the ability of the protein to interact with  
304 altiratinib. Using an indirect thermal shift assay and a thermophoresis approach (Fig. 4, F to H),  
305 we demonstrated that the hydrophobic stacking of W649 is essential for altiratinib binding, as  
306 almost no stabilization is observed in the presence of altiratinib ( $\Delta T_m$  of 3  $^{\circ}$ C), compared  
307 to WT PRPF4B ( $\Delta T_m$  of 11 $^{\circ}$ C, Fig. 3A), while the apparent  $K_d$  measured in  
308 thermophoresis transitions from 64 nM to not measurable (Fig. 3B and Fig. 4G).

309

310 Finally, we tested these sets of recombinant wild-type and mutant *TgPRP4K* proteins to assess  
311 the inhibitory effect of altiratinib on *in vitro* endpoint kinase activity using a reporter assay for  
312 ATP content and PRP31 peptide as substrate. In this context, WT *TgPRP4K* shows measurable  
313 kinase activity and exhibits the highest sensitivity to altiratinib with an apparent IC50 of 13 nM  
314 (Fig. 4i). The L715F mutant binds with higher affinity to altiratinib but is significantly less  
315 sensitive with an apparent IC50 of 62 nM. The W649P mutation brings the greatest tolerance  
316 to altiratinib, as the apparent IC50 now ranges at more than 300 nM (Fig. 4i).

317

### 318 **Chemically induced inactivation of *TgPRP4K* activity disturbs pre-mRNA splicing in *T.*** 319 ***gondii***

320 Since it has been proposed that the human kinase PRPF4B and *PfCLK3* regulate RNA splicing  
321 (8, 10), we examined transcriptional changes in the parental parasite RH and in the drug-  
322 resistant strains L715F and W649P in response to exposure to altiratinib using nanopore long-  
323 read direct RNA sequencing (DRS), a technology well suited for determining the full repertoire  
324 of mRNA species, including alternative splicing isoforms and divergent patterns, if present.  
325 The most obvious effect was that a substantial number of genes (n=2400) showed altered  
326 mRNA expression, of which 784 were induced and 1616 repressed when the parent strain was  
327 treated with altiratinib, whereas no significant changes were observed in the two mutant strains  
328 exposed to the drug (Fig. 5A). This confirms that altiratinib disrupts mRNA transcription,  
329 which was expected, but also that the drug specifically targets *TgPRP4K*, as both mutations not  
330 only confer resistance (Fig. 2, D to F) but also restore gene expression to the untreated state

331 (Fig. 5A). Having identified isoforms with high confidence using the Nanopore data, we used  
332 FLAIR (Full-Length Alternative Isoform Analysis of RNA) (25) as a framework for analyzing  
333 differential isoform usage in wild-type and mutant strains left untreated or exposed to altiratinib.  
334 The most important transcriptional phenotype was the change in pre-mRNA splicing dynamics  
335 associated with inhibition of *TgPRP4K* exclusively in WT parasites (Fig. 5B). At many *loci*,  
336 chemical inactivation of *TgPRP4K* was accompanied by complete retention of the second intron  
337 (e.g., *TGME49\_214940*; Fig. 5, B and D) or intron retention and exon skipping at the same *loci*  
338 (e.g., *TGME49\_211420* and *TGME49\_247350*; Fig. 5C; Fig. S11A). When an intron is spliced,  
339 it rapidly promotes splicing of subsequent introns, whereas when splicing is hindered,  
340 subsequent introns tend to be retained, leading to the concept of ‘all or none’ splicing (26, 27).  
341 Consistent with this concept, we regularly observed a global collapse of splicing along the entire  
342 transcript (e.g., *TGME49\_208450*; Fig. S11B) after drug treatment.

343

344 Since splicing is predominantly co-transcriptional, we also observed that intron retention leads  
345 to premature transcriptional termination (e.g., *TGME49\_278940*; Fig. S11C). At the  
346 transcriptome level, intron retention is the predominant aberrant splicing event found in  
347 altiratinib-treated WT tachyzoites in contrast to the host cells they infect, underscoring the high  
348 degree of selectivity of altiratinib (Fig. 5E). Upon closer inspection, we found that intron  
349 retention leads to premature termination of translation due to frameshifts, which may ultimately  
350 lead to altered function of the protein-coding gene. In addition, aberrant isoforms are degraded,  
351 as indicated by the lower read rates at some *loci*, likely through nonsense-mediated decay  
352 (NMD), a quality control mechanism that eliminates transcripts with a premature termination  
353 codon. In this way, treatment with altiratinib leads to the production of defective proteins that  
354 ultimately affect parasite survival.

355

### 356 **Altiratinib also causes mis-splicing in *P. falciparum* but not in *C. parvum*, which has a** 357 **divergent PRP4K ortholog**

358 Because altiratinib was active against a wide range of apicomplexans (Fig. 1) and the  
359 PRPK4/CLK3 family was well conserved within the phylum, we wondered whether the drug  
360 might inhibit splicing in other parasites of the phylum. We first examined transcriptional  
361 changes of red blood cells infected with *P. falciparum* after treatment with altiratinib using  
362 Nanopore DRS. All types of splicing defects that we had observed in *T. gondii* were also present  
363 in *P. falciparum*, such as exon skipping, intron retention, and premature transcription

364 termination (Fig. 6A; Fig. S12, A to C), with a general trend toward global splicing collapse  
365 along the entire transcript, with premature mRNAs being highly susceptible to NMD  
366 degradation (Fig. S12, A to C). As with *T. gondii*, markedly increased intron retention is a  
367 conserved phenomenon in *P. falciparum* exposed to altiratinib (Fig. 6B). These results  
368 underscore the potential targeting by altiratinib of *Pf*CLK3 (*PF3D7\_1114700*), a kinase that is  
369 essential for *P. falciparum* survival in red blood cells and plays a critical role in regulating RNA  
370 splicing of the malaria parasite (8, 9). We then took the opportunity to test the drug on  
371 *Cryptosporidium parvum*, a parasite of the phylum that differs from others in having a  
372 significantly divergent ortholog of PRP4K/CLK3 (*cgd8\_5180*, Fig. S4A), specifically the  
373 resistance-conferring DFG motif instead of the DLG motif found in *T. gondii* and *P. falciparum*,  
374 but also several significant mutations at other altiratinib-interacting residues (L719 to F, W651  
375 to H, and C713 to S) that may strongly affect the binding selectivity of altiratinib (Fig. S12, D  
376 and E). As expected, we observed no defects in mRNA splicing in *C. parvum* exposed to  
377 altiratinib (Fig. 6, C and D; Fig. S12D), again confirming the selectivity of the drug for  
378 PRP4K/CLK3 with a DLG motif and ruling out off-target activities (Fig. S12E).

379

### 380 **Assessing the ins and outs of CLK3/PRP4K inhibition by altiratinib or TCMDC-135051**

381 To further confirm *P. falciparum* *Pf*CLK3/PRP4K as a target of altiratinib, we expressed the  
382 WT *Pf*PRP4K kinase domain to probe this biochemical interaction (Fig. S13A). Using the  
383 previously described thermal shift assay, we found that altiratinib indeed stabilizes *Pf*CLK3,  
384 albeit with a weaker potential, the delta T<sub>m</sub> is of 4°C, compared to *Tg*PRP4K, which has a delta  
385 T<sub>m</sub> of 11°C (Fig. 6E). Interestingly, however, when probing the TCMDC-135051 compound,  
386 a recently discovered inhibitor of *Pf*CLK3 (9), we observed a reversed trend with a stronger  
387 stabilizing effect on *Pf*CLK3 with a delta T<sub>m</sub> of 10°C instead of 7°C for *Tg*PRP4K (Fig. 6E).  
388 These results highlight two important aspects. First, we confirm that TCMDC-135051 likely  
389 binds the active site of *Pf*CLK3 as the energy requirements for such a stabilizing effect would  
390 probably only occur within a buried cavity strongly interacting with the compound. Second,  
391 this also highlights that there may still be some species selectivity between the two compounds.  
392 As we were unable to crystallize *Pf*CLK3 in the bound or unbound state, we used alphafold2  
393 (28) within collabfold (29) to create a model that we superposed to our crystallographic  
394 structure and manually docked TCMDC-135051, taking advantage of the structural homology  
395 to other hinge regions binders containing a 7-azaindole scaffold (Fig. S13B, as initially  
396 proposed in 9). In this modeling (Fig. 6F), we observe that most of the PRP4K/CLK3 hinge

397 region is conserved between *P. falciparum* and *T. gondii*, in particular residues W649/W651 in  
398 *TgPRP4K*, which are also fully conserved in *PfCLK3* (W446/W448) and likely also have an  
399 important impact on the selectivity of TCMDC-135051, particularly through hydrophobic  
400 stacking. However, the conformation of the activation loop is not consistent with the binding  
401 of TCMDC-135051 in the *TgPRP4K* structure (Fig. 6F), indicating potential differences in the  
402 activation loop conformation that may differ between TCMDC-135051 and altiratinib.

403

## 404 **Discussion**

405 Our studies define altiratinib as a promising apicomplexan drug candidate effective against the  
406 human pathogens *T. gondii* and, with lesser efficacy, *P. falciparum*, as well as *N. caninum* and  
407 *E. tenella* of veterinary interest. Using genetic, structural and transcriptional approaches, we  
408 have shown that repurposing of altiratinib disrupts mRNA splicing in *T. gondii* and *P.*  
409 *falciparum* by targeting the kinase core of PRP4K/CLK3. The induced splicing defects are so  
410 extensive that they lead to irreversible inhibition in the nanomolar range of rapidly proliferating  
411 apicomplexan zoites in cellular assays. Using a genetic target-deconvolution strategy, we have  
412 highlighted key residues involved in binding to altiratinib. Unexpectedly, this has allowed us  
413 to crystallize and resolve the first structure of a previously elusive apicomplexan kinase  
414 PRP4K/CLK3. This co-crystal structure allows us to assign the electron density of altiratinib,  
415 located at the interface between the N- and C-terminal lobes and occupying both the ATP-  
416 binding site and the allosteric pocket, a singular type of binding that holds PRP4K in a DFG-  
417 out conformation consistent with inhibition of the type II kinases. The structural data have  
418 clarified many unanswered questions related to the species selectivity of altiratinib, as we now  
419 know that its ability to discriminate the human ortholog and bind the parasitic PRP4K/CLK3 is  
420 constrained by residues W649/W651 in the hinge region (Fig. 4A), which have diverged  
421 significantly and are also likely critical for binding of the recently discovered *PfCLK3* inhibitor  
422 TCMDC-135051 (Fig. 6F) (8, 9). Another important divergence is the shift from DFG to DLG  
423 that has occurred between mammals and some apicomplexans. DLG is indeed associated with  
424 inactive or less active kinases such as ROR2 (30, 31), and the selective pressure that led to this  
425 mutation is not yet clear, as DFG-mutated tachyzoites behave normally in cell cultures (Fig. 2,  
426 D to F). DLF conversion to DFG results in resistance to altiratinib, both *in vivo* and *in vitro*  
427 activity assays. This observation, although counterintuitive, is not unique, as other resistance-  
428 conferring mutations in *Abl*, *RET*, and *EGFR* have been shown to promote resistance by  
429 increasing kinase activity without altering the binding properties of the drug (32-34). This likely

430 gain in activity is sufficient to resist altiratinib both *in vivo* and *in vitro*, although binding  
431 affinities are increased. Our work highlights the utility of drug repurposing and provides  
432 structural mechanistic insights into understanding how the PRP4K/CLK3 family is susceptible  
433 to selective pharmacological inhibition by small drug-like molecules. This opens new  
434 opportunities to chemically improve existing molecules to optimize pathogen killing via the  
435 PRP4K/CLK3 pathway.

436

437 However, some open questions and study limitations remain. Although the evidence for a direct  
438 interaction between altiratinib and PRP4K/CLK3 and drug-induced mis-splicing is  
439 overwhelming, the possibility that *Tg*PRP4K acts as a resistance gene cannot be ruled out.  
440 Moreover, the true mechanism of spliceosome inhibition is still in question, as PRP4K not only  
441 plays a role in pre-B spliceosome activation by phosphorylating other components of PRP,  
442 notably PRP6 and PRP31 (10), but also structurally integrates the complex (21) and contacts  
443 the RNase PRP8, which may be allosterically involved in its activity. Inhibition of activity or  
444 conformational entrapment (or both) may therefore be the key to proper inhibition.  
445 Furthermore, the *in vitro* inhibition assay had to be performed with protein concentrations  
446 higher than the apparent  $IC_{50}$  (107 nM) and display inherent differences in intrinsic activity  
447 (between wild-type and mutated recombinant *Tg*PRP4K). Although the relative distribution of  
448 the  $IC_{50_{app}}$  values confirms the trend toward resistance,  $IC_{50}$  values are influenced by  
449 stoichiometric (tight) binding kinetics and may be overestimated in this context.

450

451 Our structural model is also built on a L715F mutated *Tg*PRP4K which has provided us with a  
452 stable crystal system. While the placement of altiratinib will not change, the activation loop  
453 dynamics are probably different in the wild-type context. *Pf*CLK3 has been identified as a  
454 multistage cross-species malarial drug target and TCMDC-135051 a drug candidate with a high  
455 curative and transmission-blocking potential (8, 9). Altiratinib and TCMDC-135051 have a  
456 very different chemical space (Fig. S13B) and although they probably rely on comparable  
457 elements within the hinge region to selectively bind apicomplexan PRP4K/CLK3, species  
458 selectivity is still present, possibly due to differences in the dynamics of the activation loop  
459 with which binding is compatible. Dual (SAR)-directed optimization will therefore open the  
460 possibility of developing a pan-apicomplexan therapy based on the altiratinib/TCMDC-135051  
461 combination.

462

## 463 **Materials and Methods**

464

### 465 **Study Design**

466 This study includes three sequential phases. An *in vitro* phenotypic screen using *T. gondii*  
467 tachyzoites infecting single-layered cells to identify potent inhibitors within a small library of  
468 repurposable drugs. The second phase was to determine the inhibitory properties of the lead  
469 compound altiratinib and identify resistance-conferring genes by chemical mutagenesis of *T.*  
470 *gondii*, mapping of point mutations, and complementation in a wild-type background. The third  
471 phase was to confirm the mechanism of action of altiratinib on TgPRP4K by *in vitro* biophysical  
472 methods, experimental structural biology, and functional transcriptomics in several  
473 apicomplexan parasites cultured *in vitro*. Sample sizes were based on similar experiments in  
474 the literature and are indicated in the figure legends. Whenever possible, replicate or triplicate  
475 measurements were performed. Proteomic, transcriptomic or structural experimental data were  
476 deposited in curated databases when available. This study was not blinded.

477

478 ***Toxoplasma gondii*, *Plasmodium falciparum* and human cell culture.** Human primary  
479 fibroblasts (HFFs, ATCC® CCL-171™) were cultured in Dulbecco's Modified Eagle Medium  
480 (DMEM) (Invitrogen) supplemented with 10% heat inactivated Fetal Bovine Serum (FBS)  
481 (Invitrogen), 10 mM (4-(2-hydroxyethyl)-1-piperazine ethanesulphonic acid) (HEPES) buffer  
482 pH 7.2, 2 mM L-glutamine and 50 µg/ml of penicillin and streptomycin (Invitrogen). Cells were  
483 incubated at 37°C in 5% CO<sub>2</sub>. The *Toxoplasma* strains used in this study and listed in Table S5  
484 were maintained *in vitro* by serial passage on monolayers of HFFs. The cultures were free of  
485 mycoplasma, as determined by qualitative PCR. *P. falciparum* parasites were cultured using  
486 standard culture conditions (35). The drug sensitive laboratory strain 3D7 was used in this  
487 study.

488

489 ***Toxoplasma gondii* genome editing.** Targeted genome modifications were performed using  
490 the *T. gondii* adapted CRISPR/Cas9 system as previously described (36). Recombinant  
491 parasites harboring allelic replacement for PRP4K<sup>F647S</sup>, PRP4K<sup>L686F</sup>, PRP4K<sup>L715F</sup>, and  
492 PRP4K<sup>W649P</sup> were generated by electroporation of the *T. gondii* RH NLuc strain with  
493 pTOXO\_Cas9CRISPR vectors targeting the *PRP4K* coding sequence (sgPRP4K<sup>F647S</sup>,  
494 sgPRP4K<sup>L686F</sup>, sgPRP4K<sup>L715F</sup>) and their respective donor single-stranded oligo DNA  
495 nucleotides (ssODNs) carrying respective nucleotide substitutions (PRP4K<sup>F647S</sup>\_donor,



496 PRP4K<sup>L686F</sup>\_donor, PRP4K<sup>L715F</sup>\_donor; Table S5) for homology-directed repair. Recombinant  
497 parasites were selected with 300nM altiratinib prior to subcloning by limited dilution, and  
498 allelic replacement was verified by sequencing of *T. gondii* *TgPRP4K* genomic DNA.

499

500 ***Toxoplasma gondii* random mutagenesis.** Parasites (RH strain) were chemically mutagenized  
501 as previously described (14), with the following modifications. Briefly, ~10<sup>7</sup> tachyzoites  
502 growing intracellularly in HFF cells in a T25 flask were incubated for 4 h at 37°C in 0.1% FBS  
503 DMEM growth medium containing either 2.5 mM ethyl methanesulphonate (EMS) at final  
504 concentration or the appropriate vehicle controls. After exposure to the mutagen, parasites were  
505 washed three times with PBS, and the mutagenized population was allowed to recover in a fresh  
506 T25 flask containing an HFF monolayer in the absence of drug for 3–5 days. The released  
507 tachyzoites were then inoculated into fresh cell monolayers in medium containing 300 nM of  
508 altiratinib and incubated until viable extracellular tachyzoites emerged 8–10 days later.  
509 Surviving parasites were passaged once more under continued altiratinib treatment and cloned  
510 by limiting dilution. The cloned mutants were each isolated from 6 independent mutagenesis  
511 experiments. Thus, each flask contained unique SNV pools.

512

513 **Direct RNA sequencing by nanopore.** The mRNA library preparation followed the SQK-  
514 RNA002 kit (Oxford Nanopore) recommended protocol, the only modification was the input  
515 mRNA quantity increased from 500 to 1000 ng, all other consumables and parameters were  
516 standard. Final yields were evaluated using the Qubit HS dsDNA kit (Thermofisher Q32851)  
517 with minimum RNA preps reaching at least 150 ng. For all conditions, sequencing was  
518 performed on FLO-MIN106 flow cells either using a MinION MK1C or MinION sequencer.  
519 All datasets were subsequently basecalled with a Guppy version higher than 5.0.1 with a Qscore  
520 cutoff > 7. Long read alignment were performed by Minimap2 as previously described (37).  
521 Alignments were converted and sorted using Samtools.

522

523 **Software and Statistical analyses.** Volcano plots, scatter plots, and histograms were generated  
524 with Prism 7. Structural representations of *TgPRP4K* and *PfPRP4K/CLK3* were performed  
525 using UCSF-Chimera while the schematic representation of altiratinib interaction network was  
526 computed using Ligplot.

527

528 **List of Supplementary Materials**

529 **Supplementary Materials and Methods and references**

530 **Fig. S1.** Identification of altiratinib by a medium-throughput screening of an FDA-approved  
531 library.

532 **Fig. S2.** Chemical structures of the 14 compounds selected for their efficacy in inhibiting  
533 growth of *T. gondii*.

534 **Fig. S3.** Representation of *T. gondii* cytotoxicity after incubation with drugs.

535 **Fig. S4.** Origin and interactome of TgPRP4K.

536 **Fig. S5.** Domain architectures of proteins purified together with PRP4K and PRP8.

537 **Fig. S6.** Identification and validation of the molecular target TgPRP4K.

538 **Fig. S7.** Comparison of altiratinib resistance in EMS-mutagenized and CRISPR/Cas9-edited  
539 lines.

540 **Fig. S8.** Insect-cell recombinant expression of TgPRP4K.

541 **Fig. S9.** Crystal structure specificities of TgPRP4K.

542 **Fig. S10.** Altiratinib binding site and interaction network.

543 **Fig. S11.** DRS examples of altiratinib induced splicing defects in *Toxoplasma gondii*.

544 **Fig. S12.** DRS examples of altiratinib treatment on *P. falciparum* and *C. parvum*.

545 **Fig. S13.** Biochemistry of recombinant PfPRP4K and chemical structure comparison of  
546 altiratinib and TCMDC-135051.

547 **Table S1.** Table describing the compound library and the selected molecules.

548 **Table S2.** RNA-Seq Analysis of the EMS-Induced Drug-Resistant Lines of *T. gondii*.

549 **Table S3.** Mass spectrometry-based characterization of the interactomes of PRP4K and PRP8.

550 **Table S4.** Statistics of crystallographic data.

551 **Table S5.** Description of *T. gondii* strains, plasmids and primers.

552 **Data File 1.** Full PDB X-ray structure validation report of crystal structure of *Toxoplasma*  
553 TgPRP4K with altiratinib (pdb id: 7Q4A).

554

555 **References and Notes**

556 1. WHO. World Malaria Report 2021. Who vol. 73 (2021).

557 2. J. G. Montoya, O. Liesenfeld, Toxoplasmosis. *Lancet* **363**, 1965–1976 (2004).

558 3. I. R. Dunay, K. Gajurel, R. Dhakal, O. Liesenfeld, J. G. Montoya, Treatment of  
559 toxoplasmosis: historical perspective, animal models, and current clinical practice. *Clin.*  
560 *Microbiol. Rev.* **31**, e00057-17 (2018).

- 561 4. K. Bessoff, A. Sateriale, K. K. Lee, C. D. Huston, Drug repurposing screen reveals  
562 FDA-approved inhibitors of human HMG-CoA reductase and isoprenoid synthesis that  
563 block *Cryptosporidium parvum* growth. *Antimicrob Agents Chemother.* **57**,1804-1814  
564 (2013).
- 565 5. M. Xu, E. M. Lee, Z. Wen, Y. Cheng, W. K. Huang, X. Qian, J. Tcw, J. Kouznetsova,  
566 S. C. Ogden, C. Hammack, F. Jacob, H. N. Nguyen, M. Itkin, C. Hanna, P. Shinn, C.  
567 Allen, S. G. Michael, A. Simeonov, W. Huang, K. M. Christian, A. Goate, K. J.  
568 Brennand, R. Huang, M. Xia, G. L. Ming, W. Zheng, H. Song, H. Tang, Identification  
569 of small-molecule inhibitors of Zika virus infection and induced neural cell death via a  
570 drug repurposing screen. *Nat Med.* **22**, 1101-1107 (2016).
- 571 6. Y. Kwon, B. D. Smith, Y. Zhou, M. D. Kaufman, A. K. Godwin, Effective inhibition of  
572 c-MET-mediated signaling, growth and migration of ovarian cancer cells is influenced  
573 by the ovarian tissue microenvironment. *Oncogene* **34**, 144–153 (2015).
- 574 7. B. D. Smith, M. D. Kaufman, C. B. Leary, B. A. Turner, S. C. Wise, Y. M. Ahn, R. J.  
575 Booth, T. M. Caldwell, C. L. Ensinger, M. M. Hood, W. P. Lu, T. W. Patt, W. C. Patt,  
576 T. J. Rutkoski, T. Samarakoon, H. Telikepalli, L. Vogeti, S. Vogeti, K. M. Yates, L.  
577 Chun, L. J. Stewart, M. Clare, D. L. Flynn, Altiratinib Inhibits Tumor Growth, Invasion,  
578 Angiogenesis, and Microenvironment-Mediated Drug Resistance via Balanced  
579 Inhibition of MET, TIE2, and VEGFR2. *Mol Cancer Ther.* **9**, 2023-2034 (2015).
- 580 8. M. M. Alam, A. Sanchez-Azqueta, O. Janha, E. L. Flannery, A. Mahindra, K. Mapesa,  
581 A. B. Char, D. Sriranganadane, N. M. B. Brancucci, Y. Antonova-Koch, K. Crouch, N.  
582 V. Simwela, S. B. Millar, J. Akinwale, D. Mitcheson, L. Solyakov, K. Dudek, C. Jones,  
583 C. Zapatero, C. Doerig, D. C. Nwakanma, M. J. Vázquez, G. Colmenarejo, M. J.  
584 Lafuente-Monasterio, M. L. Leon, P. H. C. Godoi, J. M. Elkins, A. P. Waters, A. G.  
585 Jamieson, E. F. Álvaro, L. C. Ranford-Cartwright, M. Marti, E. A. Winzeler, F. J. Gamo,  
586 A. B. Tobin, Validation of the protein kinase Pf CLK3 as a multistage cross-species  
587 malarial drug target *Science* **365**(6456):eaau1682 (2019).
- 588 9. A. Mahindra, O. Janha, K. Mapesa, A. Sanchez-Azqueta, M. M. Alam, A. Amambua-  
589 Ngwa, D. C. Nwakanma, A. B. Tobin, Jamieson AG. Development of Potent PfCLK3  
590 Inhibitors Based on TCMDC-135051 as a New Class of Antimalarials. *J Med Chem.*  
591 **63**, 9300-9315 (2020).
- 592 10. M. Schneider, H. H. Hsiao, C. L. Will, R. Giet, H. Urlaub, R. Lührmann, Human PRP4  
593 kinase is required for stable tri-snRNP association during spliceosomal B complex  
594 formation. *Nat Struct Mol Biol.* **17**, 216-221 (2010).

- 595 11. M. Lützelberger, N. F. Käufer, The Prp4 Kinase: Its Substrates, Function and  
596 Regulation in Pre-mRNA Splicing. In: Dr. Huang Cai (Ed.), editor. Protein  
597 Phosphorylation in Human Health: InTech. (2012).
- 598 12. D. P. Corkery, A. C. Holly, S. Lahsae, G. Dellaire, Connecting the speckles: Splicing  
599 kinases and their role in tumorigenesis and treatment response. *Nucleus* **6**, 279-88  
600 (2015).
- 601 13. D. Eckert, N. Andrée, A. Razanau, S. Zock-Emmenthal, M. Lützelberger, S. Plath, H.  
602 Schmidt, A. Guerra-Moreno, L. Cozzuto, J. Ayté, N. F. Käufer, Prp4 Kinase Grants the  
603 License to Splice: Control of Weak Splice Sites during Spliceosome Activation. *PLoS*  
604 *Genet.* **12**, e1005768 (2016).
- 605 14. V. Bellini, C. Swale, M. P. Brenier-Pinchart, T. Pezier, S. Georgeault, F. Laurent, M.  
606 A. Hakimi, A. Bougdour, Target Identification of an Antimalarial Oxaborole Identifies  
607 AN13762 as an Alternative Chemotype for Targeting CPSF3 in Apicomplexan  
608 Parasites. *iScience.* **23**, 101871 (2020).
- 609 15. E. Talevich, A. Mirza, N. Kannan, Structural and evolutionary divergence of eukaryotic  
610 protein kinases in Apicomplexa. *BMC Evol. Biol.* **11**, 321 (2011).
- 611 16. Z. Zhou, X. D. Fu, Regulation of splicing by SR proteins and SR protein-specific  
612 kinases. *Chromosoma* **122**, 191–207 (2013).
- 613 17. S. Agarwal, S. Kern, J. Halbert, J. M. Przyborski, S. Baumeister, T. Dandekar, C.  
614 Doerig, G. Pradel, Two nucleus-localized CDK-like kinases with crucial roles for  
615 malaria parasite erythrocytic replication are involved in phosphorylation of splicing  
616 factor. *J. Cell. Biochem.* **112**, 1295–1310 (2011).
- 617 18. S. M. Sidik, D. Huet, S. M. Ganesan, M. H. Huynh, T. Wang, A. S. Nasamu, P. Thiru,  
618 J. P. J. Saeij, V. B. Carruthers, J. C. Niles, S. Lourido, A Genome-wide CRISPR Screen  
619 in Toxoplasma Identifies Essential Apicomplexan Genes. *Cell.* **166**, 1423-1435 (2016).
- 620 19. V. V. Lee, S. Seizova, P. J. McMillan, E. McHugh, C. J. Tonkin, S. A. Ralph,  
621 Identification and characterisation of splicing regulators in Toxoplasma gondii.  
622 <https://www.biorxiv.org/content/10.1101/2021.06.27.450092v3>
- 623 20. C. A. Bottner, H. Schmidt, S. Vogel, M. Michele, N. F. Käufer, Multiple genetic and  
624 biochemical interactions of Brr2, Prp8, Prp31, Prp1 and Prp4 kinase suggest a function  
625 in the control of the activation of spliceosomes in Schizosaccharomyces pombe. *Curr*  
626 *Genet.* **48**, 151-61 (2005).
- 627 21. C. Charenton, M. E. Wilkinson, K. Nagai, Mechanism of 5' splice site transfer for  
628 human spliceosome activation. *Science.* **364**, 362-367 (2019).

- 629 22. K. Bertram, D. E. Agafonov, O. Dybkov, D. Haselbach, M. N. Leelaram, C. L. Will, H.  
630 Urlaub, B. Kastner, R. Lührmann, H. Stark, Cryo-EM Structure of a Pre-catalytic  
631 Human Spliceosome Primed for Activation. *Cell* **170**, 701–713 (2017).
- 632 23. G. Dellaire, E. M. Makarov, J. J. Cowger, D. Longman, H. G. Sutherland, R. Lührmann,  
633 J. Torchia, W. A. Bickmore, Mammalian PRP4 kinase copurifies and interacts with  
634 components of both the U5 snRNP and the N-CoR deacetylase complexes. *Mol Cell*  
635 *Biol.* **22**, 5141-5156 (2002).
- 636 24. E. A. Greene, C. A. Codomo, N. E. Taylor, J. G. Henikoff, B. J. Till, S. H. Reynolds,  
637 L. C. Enns, C. Burtner, J. E. Johnson, A. R. Odden, L. Comai, S. Henikoff. Spectrum  
638 of chemically induced mutations from a large-scale reverse-genetic screen in  
639 *Arabidopsis*. *Genetics* **164**, 731–740 (2003).
- 640 25. A. D. Tang, C. M. Soulette, M. J. van Baren, K. Hart, E. Hrabeta-Robinson, C. J. Wu,  
641 A. N. Brooks, Full-length transcript characterization of SF3B1 mutation in chronic  
642 lymphocytic leukemia reveals downregulation of retained introns. *Nat Commun.* **11**,  
643 1438 (2020).
- 644 26. F. C. Oesterreich, L. Herzel, K. Straube, K. Hujer, J. Howard, K. M. Neugebauer,  
645 Splicing of nascent RNA coincides with intron exit from RNA polymerase II. *Cell*, **165**,  
646 372–381 (2016).
- 647 27. L. Herzel, K. Straube, K. M. Neugebauer, Long-read sequencing of nascent RNA  
648 reveals coupling among RNA processing events. *Genome Res.*, **28**, 1008–1019 (2018).
- 649 28. J. Jumper, R. Evans, A. Pritzel, T. Green, M. Figurnov, O. Ronneberger, K.  
650 Tunyasuvunakool, R. Bates, A. Žídek, A. Potapenko, A. Bridgland, C. Meyer, S. A. A.  
651 Kohl, A. J. Ballard, A. Cowie, B. Romera-Paredes, S. Nikolov, R. Jain, J. Adler, T.  
652 Back, S. Petersen, D. Reiman, E. Clancy, M. Zielinski, M. Steinegger, M. Pacholska,  
653 T. Berghammer, S. Bodenstein, D. Silver, O. Vinyals, A. W. Senior, K. Kavukcuoglu,  
654 P. Kohli, D. Hassabis, Highly accurate protein structure prediction with AlphaFold.  
655 *Nature.* **596**, 583-589 (2021).
- 656 29. M. Mirdita, S. Ovchinnikov, M. Steinegger, ColabFold - Making protein folding  
657 accessible to all. <https://www.biorxiv.org/content/10.1101/2021.08.15.456425v1>  
658 (2021).
- 659 30. S. C. Artim, J. M. Mendrola, M. A. Lemmon, Assessing the range of kinase  
660 autoinhibition mechanisms in the insulin receptor family. *Biochem J.* **448**, 213-220  
661 (2012).

- 662 31. J. M. Mendrola, F. Shi, J. H. Park, M. A. Lemmon, Receptor tyrosine kinases with  
663 intracellular pseudokinase domains. *Biochem Soc Trans.* **41**, 1029-1036 (2013).
- 664 32. C. H. Yun, T. J. Boggon, Y. Li, M. S. Woo, H. Greulich, M. Meyerson, M. J. Eck,  
665 Structures of lung cancer-derived EGFR mutants and inhibitor complexes: mechanism  
666 of activation and insights into differential inhibitor sensitivity. *Cancer Cell.* **11**, 217-27  
667 (2007).
- 668 33. T. Nakaoku, T. Kohno, M. Araki, S. Niho, R. Chauhan, P. P. Knowles, K. Tsuchihara,  
669 S. Matsumoto, Y. Shimada, S. Mimaki, G. Ishii, H. Ichikawa, S. Nagatoishi, K.  
670 Tsumoto, Y. Okuno, K. Yoh, N. Q. McDonald, K. A. Goto, A secondary RET mutation  
671 in the activation loop conferring resistance to vandetanib. *Nat Commun.* **9**, 625 (2018).
- 672 34. M. Hoemberger, W. Pitsawong, D. Kern, Cumulative mechanism of several major  
673 imatinib-resistant mutations in Abl kinase. *Proc Natl Acad Sci U S A.* **117**, 19221-19227  
674 (2020).
- 675 35. W. Trager, J. B. Jensen, Human malaria parasites in continuous culture. *Science* **193**,  
676 673–675 (1976).
- 677 36. D. C. Farhat, C. Swale, C. Dard, D. Cannella, P. Ortet, M. Barakat, F. Sindikubwabo,  
678 L. Belmudes, P. J. De Bock, Y. Couté, A. Bougdour, M. A. Hakimi, A MORC-driven  
679 transcriptional switch controls Toxoplasma developmental trajectories and sexual  
680 commitment. *Nat Microbiol.* **5**, 570-583 (2020).
- 681 37. D. C. Farhat, M. W. Bowler, G. Communie, D. Pontier, L. Belmudes, C. Mas, C. Corrao,  
682 Y. Couté, A. Bougdour, T. Lagrange, M. A. Hakimi, C. Swale, A plant-like mechanism  
683 coupling m6A reading to polyadenylation safeguards transcriptome integrity and  
684 developmental gene partitioning in Toxoplasma. *Elife.* **10**, e68312 (2021).

685

686 **Acknowledgments.** This work was supported by the Laboratoire d'Excellence (LabEx)  
687 ParaFrap [ANR-11-LABX-0024], the Agence Nationale pour la Recherche [Project HostQuest,  
688 ANR-18-CE15-0023, Project ApiNewDrug, ANR-21-CE35-0010-01, Project EpiKillMal,  
689 ANR-20-CE18-0006], the European Research Council [ERC Consolidator Grant N°614880  
690 Hosting TOXO to M.A.H], and Fondation pour la Recherche Médicale [FRM Equipe #  
691 EQU202103012571] and Roux-Cantarini Fellowship attributed to FN. The proteomic  
692 experiments were partially supported by Agence Nationale de la Recherche under projects  
693 ProFI (Proteomics French Infrastructure, ANR-10-INBS-08) and GRAL, a program from the  
694 Chemistry Biology Health (CBH) Graduate School of University Grenoble Alpes (ANR-17-

695 EURE-0003). The HTX Lab (EMBL Grenoble) are thanked for support in screening for crystal  
696 conditions and automatic mounting of crystals. **Author Contributions.** M.-A.H. led the  
697 research and coordinated the collaboration. M.-A.H. A.B. and C.S. designed the project. Y.C.  
698 and L.B. performed the mass spectrometric analyzes. F.L. designed and performed experiments  
699 on *Eimeria* and *Cryptosporidium*. A.S. and F.N. designed and performed experiments on  
700 *Plasmodium falciparum*. A.B. computed and analyzed the RNA-seq data. V.B. performed the  
701 drug screening. V.B. and D. C. performed the in vitro studies with *T. gondii*. M.-P.B.-P. and  
702 V.B. designed and performed the in vivo experiments with *T. gondii*. C.S. and MWB performed  
703 structural studies. C.S. and C.M. performed the MST and SEC-MALLS. C.S. performed  
704 nanopore DRS and analyzed them. V.B. and C.S. designed and performed biochemical studies.  
705 M.-A.H., A.B., and C.S. interpreted the experimental work and wrote the paper with editorial  
706 support from V.B. and fruitful comments from all other authors. **Data availability.** All data  
707 associated with this study are in the paper or the Supplementary Materials. All unique and stable  
708 reagents generated in this study are available by contacting M.A.H. and completion of a  
709 materials transfer agreement. The Nanopore RNAseq data have been deposited in NCBI's SRA  
710 data PRJNA774463. The Illumina RNA-seq dataset generated during this study is available at  
711 NCBI GEO: GSE193614. The coordinates and structure factors for the *TgPRP4k/altiratinib*  
712 structure have been deposited in the PDB with the accession number 7Q4A. The mass  
713 spectrometry proteomics data were deposited with the ProteomeXchange Consortium via the  
714 PRIDE partner repository with the record identifier : pxd029455. **Declaration of Interests.**  
715 The authors declare no competing interests.

716

## 717 **Figures caption.**

718

719 **Fig. 1. Efficacy of altiratinib against the parasite *Toxoplasma gondii*.** (A) Graphical  
720 representation of data from the medium-throughput screen. A cutoff was set at 70% of parasite  
721 inhibition. Red dots, hits. The workflow used for the screening is shown in **Fig. S1A**. (B) The  
722 half-maximal effective concentration (EC<sub>50</sub>) values of the 14 molecules validated at 1 μM. Data  
723 are presented as mean ± standard deviation (SD) of n=3 technical replicates. Error bars  
724 correspond to 95% confidence intervals. (C) Chemical structure of altiratinib. (D) EC<sub>50</sub> values  
725 for pyrimethamine and altiratinib. The confluent HFF monolayer was infected with tachyzoites  
726 of the *T. gondii* RH\_NanoLucEmGFP strain (Table S5). The EC<sub>50</sub> values of each biological  
727 replicate were determined by non-linear regression analysis. EC<sub>50</sub> data are presented as mean

728 G SD from 3 independent biological replicates, each with 3 technical replicates. (E) Compound  
729 efficiency presented by IFA. Confluent HFFs were infected with *T. gondii*  
730 RH\_NanoLucEmGFP and incubated with 1 $\mu$ M of pyrimethamine, 300 nM of altiratinib or  
731 0.1% of the vehicle (DMSO) for 24h. Fixed cells were stained with anti-inner membrane  
732 complex protein (GAP45) antibody (magenta). In green the cytosolic GFP. Scale bar  
733 corresponds to 5 $\mu$ m. (F) Dose-response curves of HFFs, ARPE-19, MCF7, MDA231 and U937  
734 cell lines in the presence of altiratinib. Human cells were plated out and incubated with  
735 increasing concentrations of the drug. After 72h, cell viability was determined using the  
736 “CellTiter-Blue Assay” kit (Promega) and cell cytotoxicity concentration (CC50) was  
737 calculated. The graph is representative of two different experiments performed in triplicate. The  
738 shaded error envelopes indicate 95% confidence intervals. On the right, CC50 values show the  
739 mean of two experiments. Selectivity index (SI) is based on the average of human CC50 divided  
740 by the average of *T. gondii* EC50. (G) Effect concentration curve of *Eimeria tenella* in presence  
741 of altiratinib. (H) Altiratinib inhibition of *Neospora caninum* proliferation shown by plaque  
742 assay. After 7 days of infection and drugs incubation, the size of at least 50 plaques were  
743 measured. n.d., not detected. (I) Dose-response curves of altiratinib and dihydroartemisinin  
744 (DHA) in *P. falciparum* asexual blood-stage. Graph is representing the mean and SD values  
745 obtained in three independent experiments run in triplicate.

746

747 **Fig. 2. Deconvolution and validation of the TgPRP4K molecular target.** (A) Circos plot  
748 summarizing the single nucleotide variants (SNVs) detected by transcriptomic analysis of *T.*  
749 *gondii* altiratinib-resistant lines, grouped by chromosome (numbered in Roman numerals with  
750 size intervals indicated on the outside). Each dot in the six innermost gray tracks corresponds  
751 to a scatter plot of the mutations identified in the six drug-resistant strains, with each ring  
752 representing one of the six drug-resistant lines (A through F). Each bar in the outermost track  
753 represents the positions of selected archetypal essential genes. See Table S2 for transcriptomic  
754 analysis. (B) Schematic representation of the TgPRP4K protein structure. The kinase domain is  
755 predicted in the C-terminal portion of the protein. Phosphorylated and acetylated residues are  
756 shown as blue and red dots, respectively. The orange dots correspond to the three discovered  
757 SNVs located in the kinase domain. (C) The nuclear location of TgPRP4K (red) in human  
758 primary fibroblasts (HFFs) infected with parasites expressing an HA-Flag-tagged copy of  
759 TgPRP4K. Cells were co-stained with Hoechst DNA-specific dye (blue) and the anti-Inner  
760 Membrane Complex (IMC) (green) antibody. Scale bar, 5  $\mu$ m. (D) Graphs representing the  
761 essentiality of TgPRP4K protein assessed by plaque assay. RH\_Tir1-Ty and TgPRP4K KD



762 parasites were either untreated or treated with IAA for 7 days and the size of 42 plaques were  
763 measured upon detection. n.d., not detected. (E) Fluorescence microscopy showing intracellular  
764 growth of WT and the *TgPRP4K* edited parasites (F647S, L686F, L715F). HFF cells were  
765 infected with tachyzoites of the indicated *T. gondii* strains expressing the NLuc-P2A-EmGFP  
766 reporter gene and incubated with 300 nM of altiratinib or 0.1% DMSO as control. Cells were  
767 fixed 24 h post-infection and then stained with antibodies against the *T. gondii* inner membrane  
768 complex protein GAP45 (magenta). The cytosolic GFP is shown in green. Scale bars represent  
769 5  $\mu\text{m}$ . (F)  $\text{EC}_{50}$  values for pyrimethamine (Pyr) and altiratinib were determined for WT and the  
770 engineered *TgPRP4K* mutant strains (F647S, L686F, L715F). The  $\text{EC}_{50}$  values on the upper  
771 part of the graphs represent the mean  $\pm$  SD of three biological replicates. On the top of each  
772 panel, lines shown the fold change in  $\text{EC}_{50}$  relative to that of the WT parasites. Dose-response  
773 curves are shown in Fig. S6C. (G) Effects of *TgPRP4K* mutations on *T. gondii* lytic cycle as  
774 determined by plaque assay. Plaque sizes ( $n = 50$  per condition) were measured for WT and the  
775 engineered *TgPRP4K* mutant strains (F647S, L686F, L715F) after 7 days of growth in the  
776 absence or presence of 300 nM of altiratinib. n.d., not detected. Significance was assessed by  
777 Mann-Whitney or Kruskal-Wallis tests (One-way ANOVA).

778

779 **Fig. 3. Structure of the complex *TgPRP4K*-altiratinib and mechanism of action.** (A)  
780 Thermal stability profile of WT (upper panel) and L715F (bottom panel) recombinant proteins.  
781 Each protein was incubated for 3 minutes at different temperatures (from 30° to 69° C) in  
782 presence or absence of Altiratinib (100  $\mu\text{M}$ ) to quantify the melting temperatures using non-  
783 linear regression analysis of normalized data and assuming a sigmoidal dose response. (B)  
784 Protein–Ligand interaction. WT and L715F recombinant proteins labelled to His-fluorescent  
785 dye (100 nM), were incubated with altiratinib from 0.15 nM to 5000 nM. Changes in  
786 thermophoresis were plotted as mean changes in  $F_{\text{norm}}$  values against ligand concentration,  
787 yielding a  $K_d$  of  $64 \pm 20$  nM for WT (upper panel) and  $26 \pm 2$  nM for L715F (bottom panel).  
788 Curve 95% confidence intervals are displayed;  $n = 3$ . (C) Full structure of *TgPRP4K* (L715F)  
789 bound to altiratinib (pdb id: 7Q4A). PRP4K is represented in a cartoon fashion with a  
790 transparent surface background with alpha helices colored in orange and beta strands colored  
791 in yellow. The activation loop is highlighted in blue, the DFG backbone is shown in pink, the  
792 phosphor-serine 729 side chain and altiratinib are shown in a stick representation and colored  
793 in grey and cyan respectively. (D) Altiratinib binding within *TgPRP4K*. Zoomed in focus on  
794 altiratinib and the key interacting side chains of *TgPRP4K* shown as grey sticks. Cartoon colors

795 are the same as used in panel a. (E) Sequence alignment of altiratinib *TgPRP4K* binding regions  
796 compared against *Plasmodium falciparum* (*Pf*), *Chromera Velia* (*cc*), *Schizosaccharomyces*  
797 *pombe* (*Sp*), *Arabidopsis thaliana* (*At*) and *Homo sapiens* (*Hs*) PRP4K/CLK3 orthologs. Key  
798 regions are highlighted by pink rectangles, altiratinib interacting amino acids from *TgPRP4K*  
799 are shown by cyan circles while divergent residues in the human ortholog are shown by red  
800 triangles. Mutations found in the mutagenesis experiment are highlighted by a green star. The  
801 alignment was generated with CLC sequence viewer 7.

802

803 **Fig. 4. Hinge region selectivity towards altiratinib.** (A) Hinge region species selectivity  
804 towards altiratinib. Cartoon diagram of structurally superposed *TgPRP4K* (tan) and human  
805 PRPF4B (sky blue) with altiratinib in cyan. Hinge region residues are detailed by including  
806 stick representations of their side chains. (B) Sanger chromatogram validating the *TgPRP4K*  
807 gene editing for W649P mutation. On the top, nucleotide positions relative to the ATG start  
808 codon on genomic DNA are indicated. (C) IFA showing the W649P resistance to altiratinib.  
809 Confluent HFFs were infected with engineered parasites and incubated with pyrimethamine (1  
810  $\mu\text{M}$ ) or altiratinib (300 nM) for 24h. Fixed cells were stained using anti-GAP45 antibody  
811 (magenta) while the cytosolic GFP is showed in green. Scale bar represents 5  $\mu\text{m}$ . (D) Graph  
812 representing the  $\text{EC}_{50}$  of W649P for pyrimethamine and altiratinib. Values showed in the upper  
813 part on the graph are the mean  $\pm$  SD of three independent experiment. On the top of the panel,  
814 the line shows the fold change in altiratinib  $\text{EC}_{50}$  relative to pyrimethamine. (E) Plaque assay  
815 representing the lytic cycle of RH WT and W649P parasites in presence or absence of 300 nM  
816 of altiratinib. After 7days of drugs incubation, infected cells were fixed and stained to visualize  
817 the presence of lysis plaques (on the left). The area of 50 plaques was measured and represented  
818 in the right panel. (F) Thermal stability profile of W649P recombinant protein in presence or  
819 absence of Altiratinib (100  $\mu\text{M}$ ). (G) Protein-ligand interaction profile of W649P protein in  
820 presence of Altiratinib as measured by thermophoresis with the same assay used in Fig. 3b.  
821 Changes in thermophoresis of the mean of three replicates were plotted. Curve 95% confidence  
822 intervals are displayed as dotted lines. NA, not available. (H) Table showing the melting  
823 temperature ( $T_m$ ) of WT, L715F and W649P recombinant proteins during their incubation with  
824 DMSO or Altiratinib (100  $\mu\text{M}$ ) at different temperatures. Low interaction between W649P and  
825 the compound was detected as showed by the  $\Delta T_m$  values. (I) Kinase activity inhibition *in*  
826 *vitro*. KinaseGlo® remaining ATP levels were measured and normalized for every condition.

827 The normalized endpoint activity is plotted against altiratinib concentrations. 4-parameter  
828 inhibition curves were used to determine an apparent IC<sub>50</sub> for WT, L715F and W649P mutant.  
829

830 **Fig. 5. Nanopore DRS analysis of altiratinib-induced splicing defects in *T. gondii*.** (A)  
831 General transcriptomic effects of altiratinib treatment. *k*-means clustering of 2400 transcripts  
832 treated with EdgeR: log<sub>2</sub>(CPM+4). The color key ranges from -3 to 3 (green to red), 3 clusters  
833 were defined. In each, *TgPRP4K* WT/L715F/W649P duplicate sequencing experiments are  
834 shown in the presence (300 nM) or absence of altiratinib. (B) M-pileup representation of the  
835 aligned nanopore reads at the *TGME49\_214940* loci. WT/L715F/W649P sequencing  
836 experiments are shown as grayscale histograms in the presence (300 nM) or absence of  
837 altiratinib. (C and D), FLAIR analysis of *TGME49\_211420* (C) and *TGME49\_214940* (D) loci.  
838 Standard annotation and FLAIR collapsed isoforms (FCI) are shown schematically under a  
839 sample view of 15 reads per condition (same conditions as in B). Sense and antisense reads are  
840 colored red and blue, respectively. Below the FCI representation is an isoform quantification  
841 histogram showing duplicate measurements in each WT/L715F/W649P condition and in the  
842 presence (300 nM) or absence of altiratinib. The color code is the same as for the above FCI,  
843 grey histograms represent minor isoforms which not shown schematically. (E) Overall  
844 quantification of intron retention. Scatter plot of intron retention ratios (per averaged duplicate  
845 transcript) are shown for *T. gondii* and *H. sapiens*. WT/L715F/W649P strains that were  
846 untreated (in green) or treated (300 nM, in cyan) are shown, the black histogram shows the  
847 median, the whiskers show the interquartile range. Significance between the WT untreated and  
848 treated conditions was calculated using a non-parametric Friedman test.

849

850 **Fig. 6. Cross-species selectivity of altiratinib analysed by nanopore DRS.** (A) Splicing  
851 defects induced by altiratinib in *P. falciparum*. M-pileup representation of aligned nanopore  
852 reads at the *PF3D7\_0918100* and *PF3D7\_1118700* loci. Untreated (UT) or altiratinib-treated  
853 (2.5 μM) sequencing experiments are shown as grayscale histograms. Shown below are IGB  
854 samples from 10 individual aligned reads using sense (purple) and antisense (blue) coloring  
855 under UT and treated conditions. (B) Overall quantification of intron retention in *P. falciparum*.  
856 Scatter plots of intron retention ratios (per averaged duplicate transcript) are shown for  
857 untreated (in green) or altiratinib treated (in cyan) conditions, the black histogram shows the  
858 median, the whiskers show the interquartile range. Significance between the WT untreated and  
859 treated conditions was calculated using a nonparametric Mann-Whitney *t*-test. (C) Splicing  
860 consistency is maintained in *C. parvum*. M-pileup and IGB sampling of aligned reads from

861 untreated (UT) or altiratinib treated (0.5  $\mu$ M) *C. parvum* at the highly transcribed and spliced  
862 *cdg6\_4620* loci. **(D)** Overall quantification of intron retention in *C. parvum*. The same display  
863 rules as in **B.** were applied. **(E)** Thermal shift assay of TgPRP4K and PfCLK3 in the presence  
864 of altiratinib (100  $\mu$ M) or TCDM-135051 (100  $\mu$ M). A simplicate assay is shown, but the  
865 measurement was replicated. **(F)** Hinge region species selectivity towards TCMD-135051.  
866 Cartoon diagram of the structurally superposed *TgPRP4K* from this work (in tan) and the  
867 alphaflo2 predicted *PfCLK3* (dodger blue) with TCDM-135051 modelling in orange. The  
868 residues of the hinge region are also detailed by showing their side chains as stick  
869 representations.

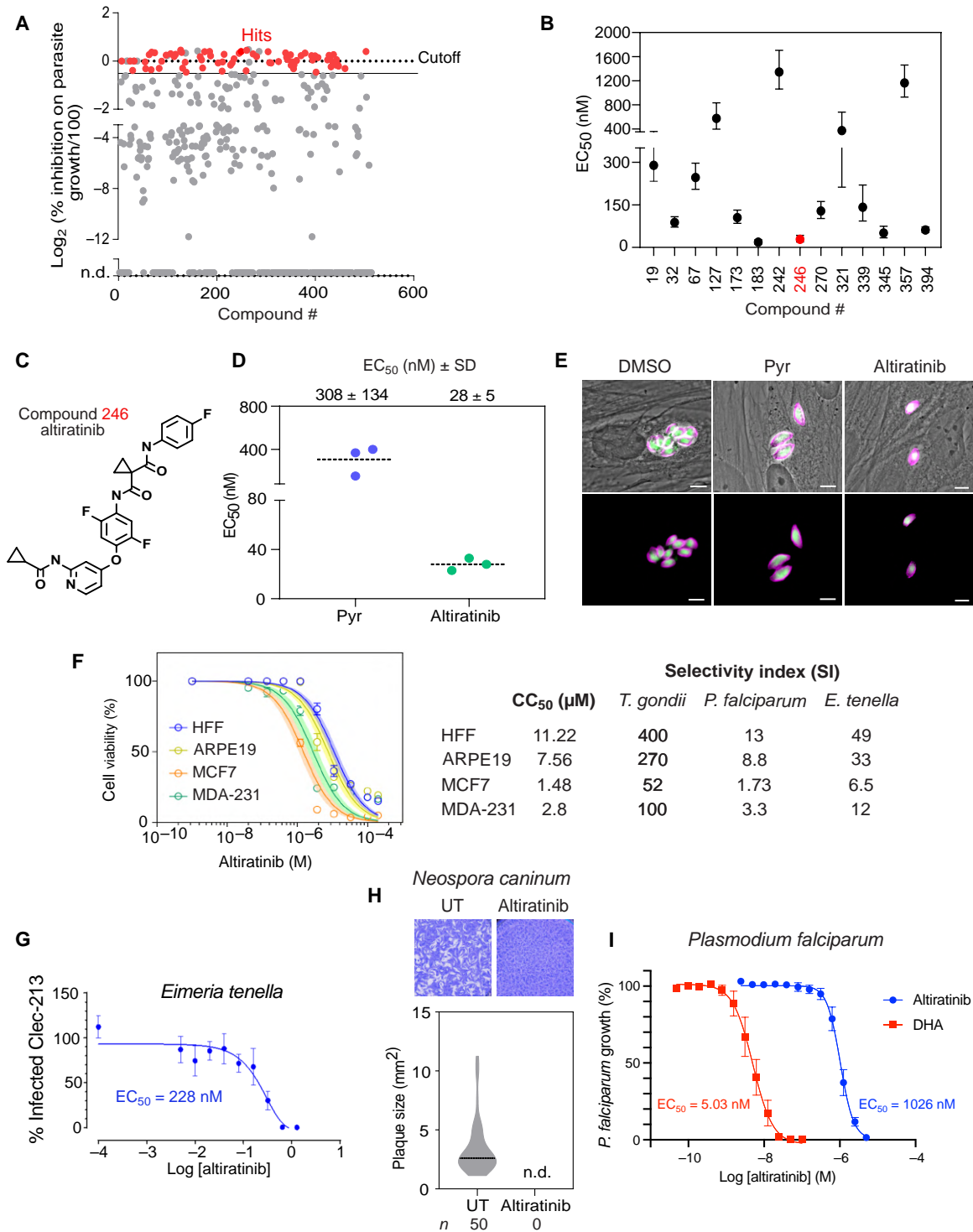
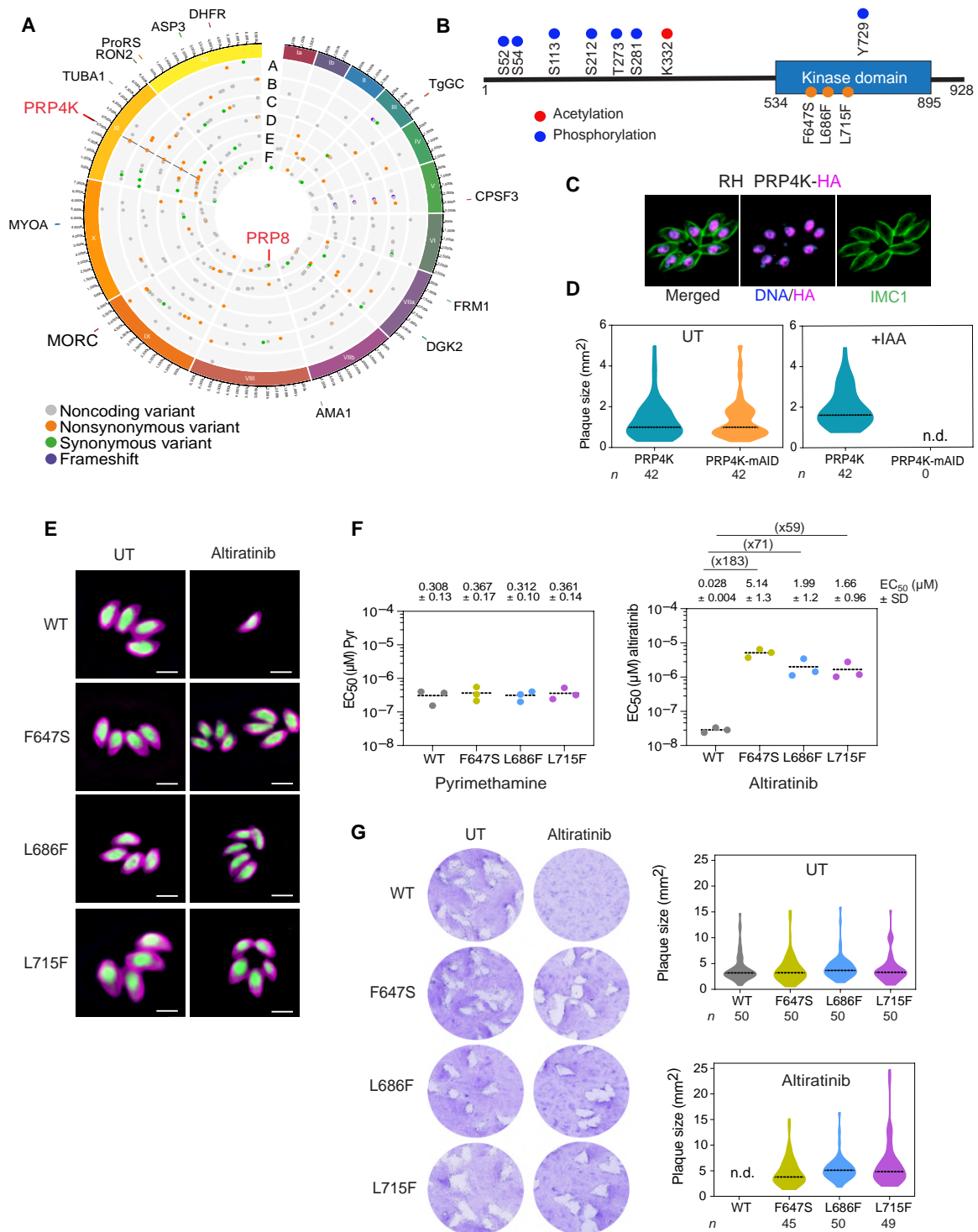


Figure 1



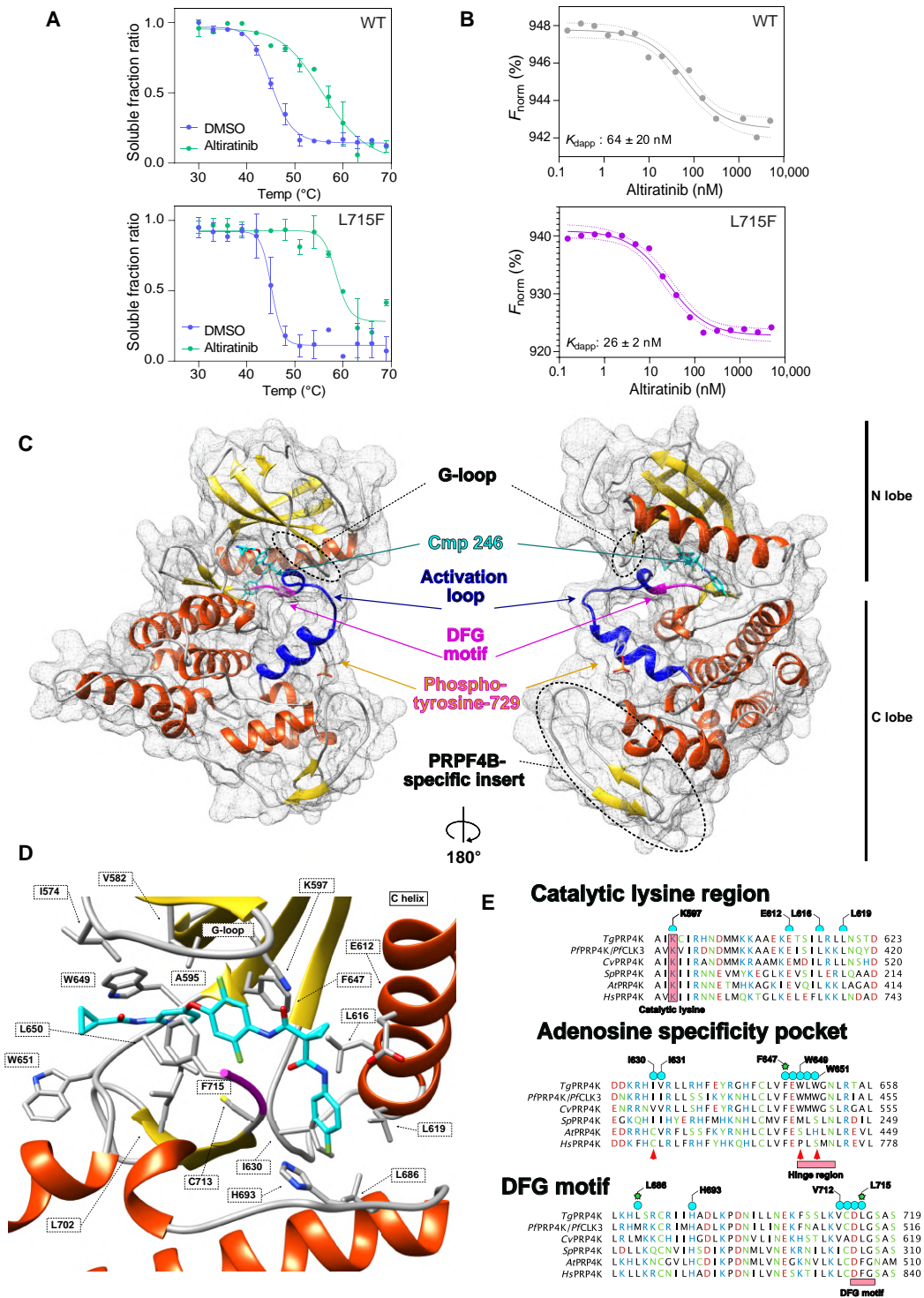


Figure 3

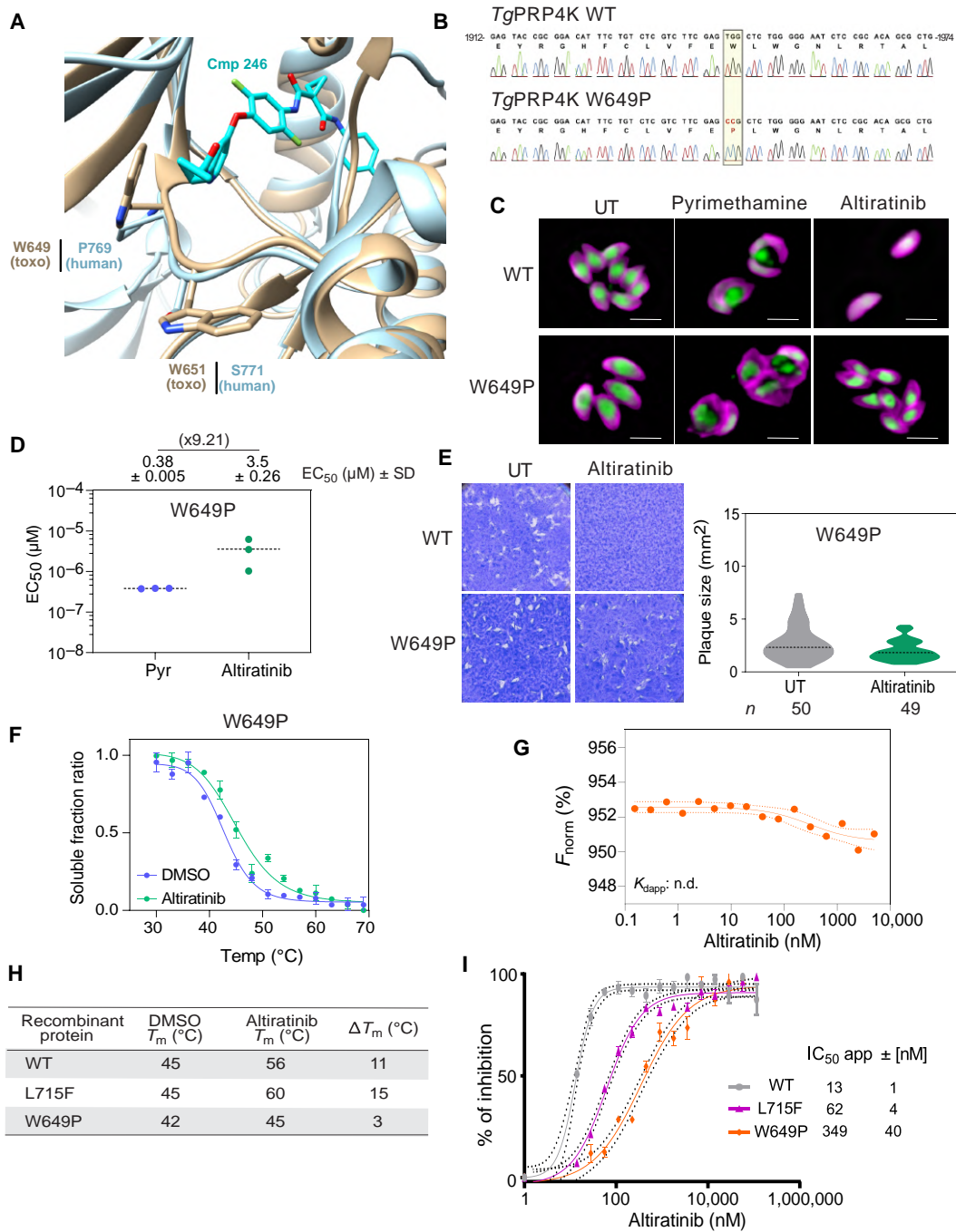


Figure 4



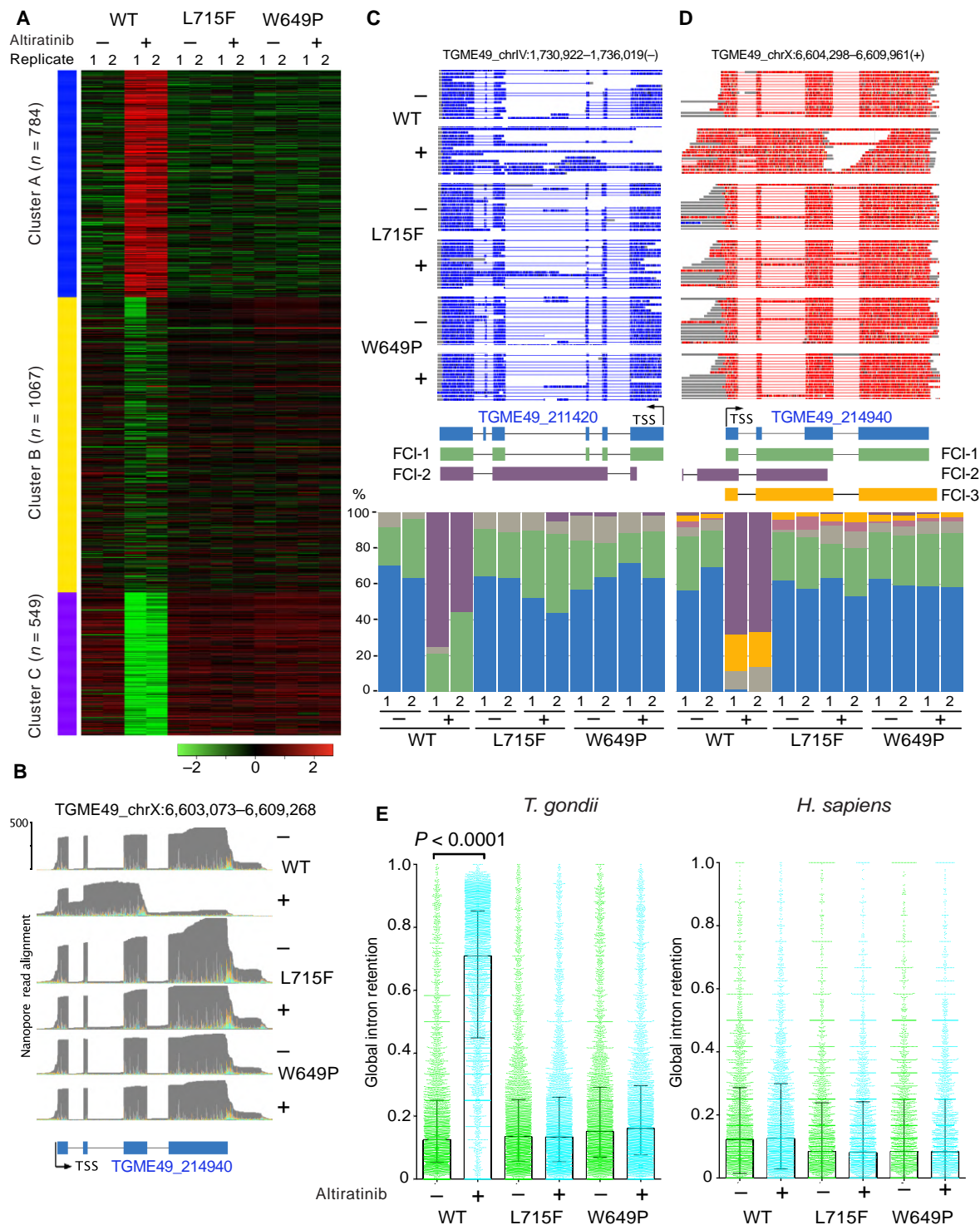


Figure 5

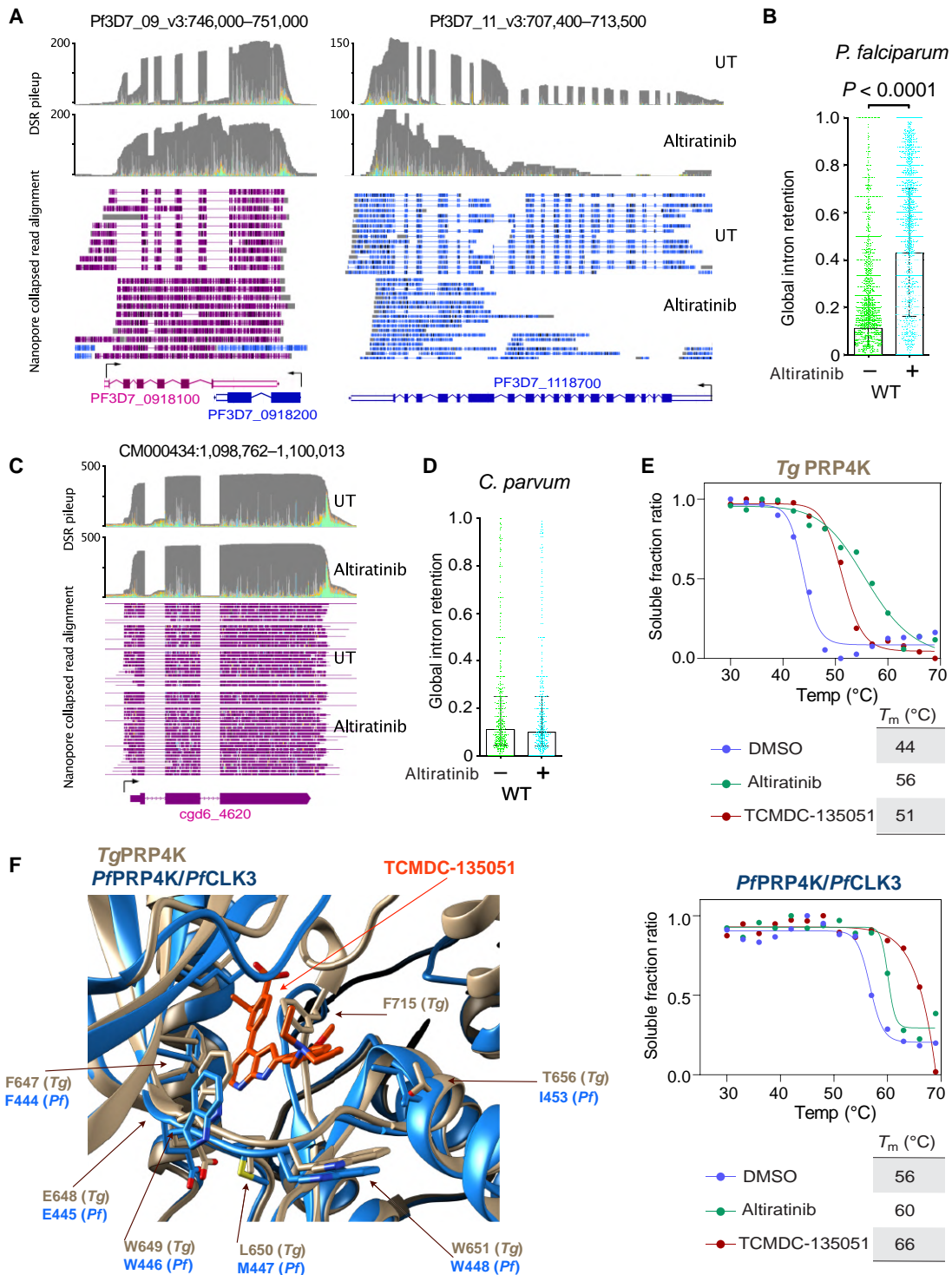


Figure 6